IRIS AperTO

UNIVERSITÀ DEGLI STUDI DI TORINO

AperTO - Archivio Istituzionale Open Access dell'Università di Torino

Designing TiO2 Based Nanostructures by Control of Surface Morphology of Pure and Silver Loaded Titanate Nanotubes

This is the author's manuscript

Original Citation:

Availability:

This version is available http://hdl.handle.net/2318/129923 since

Terms of use:

Open Access

Anyone can freely access the full text of works made available as "Open Access". Works made available under a Creative Commons license can be used according to the terms and conditions of said license. Use of all other works requires consent of the right holder (author or publisher) if not exempted from copyright protection by the applicable law.

(Article begins on next page)

01 August 2024

UNIVERSITÀ DEGLI STUDI DI TORINO

***This is an author version of the contribution published on**:*
Questa è la versione dell'autore dell'opera:

Journal of Physical Chemistry

Volume 114, Issue 1, 14 January 2010, Pages 169-178

DOI: 10.1021/jp9087207

The definitive version is available at:

http://dx.doi.org/10.1021/jp9087207

Designing TiO_2-based nanostructures by control of surface morphology of pure and silver loaded titanate nanotubes

Federico Cesano[+], *Serena Bertarione*[+], *Mohammed Jasim Uddin*[°], *Giovanni Agostini*[+], *Domenica Scarano*[+] *and Adriano Zecchina*[+]

[+]Nanostructured Interfaces and Surfaces (NIS), Centre of Excellence, Department of Chemistry IFM, University of Torino, Via P. Giuria 7, I-10125 Torino and Centre of Reference INSTM-University of Torino (Italy)

[°] current address: Tulane Univ, Dept Phys, New Orleans, LA 70118 USA

ABSTRACT: The synthesis and the morphological transformations of pure and silver loaded titanate nanotubes, into anatase titania nanostructures, under relatively mild temperatures (500°C) have been discussed. At first, it will be shown that the transformation of titanate into titanium oxide leads to the formation of TiO_2 particles, then the role of the silver, in affecting morphology, crystallinity and optical properties of the nanostructures, is highlighted. Morphology and structure of the titanate precursor and of the formed TiO_2 particles (both pure or silver loaded) have been investigated by means of BET (Brunauer-Emmett-Teller), powder XRD (X-Ray Diffraction) analyses, HRTEM (High Resolution Trasmission Electron Microscopy), AFM (Atomic Force Microscopy) and SEM (Scanning Electron Microscopy) microscopies. Surface and optical properties have been explored by means of FTIR (Fourier Transform Infrared Spectroscopy) and UV-vis (Ultra Violet - visible Diffuse Reflectance) spectroscopies. In regard to the vibrational properties of the obtained materials, the comparison of FTIR features of adsorbed CO on pure and silver exchanged titanates, with respect to pure and silver loaded TiO_2 have been reported, for the first time. It will be shown that all the materials (as prepared, either in the hydrogen or in the silver exchanged form and those obtained after thermal treatments) show better properties than the commercial TiO_2 precursor and in general than those obtained by solid state reactions (P25), in terms of specific surface area and porosity.

1. Introduction.

Since the discovery of carbon nanotubes,[1] as novel materials with properties not found in conventional graphite or carbon fullerene, much research has been conducted on developing nanotubes of various materials by controlling the nanostructures. In particular, inorganic nanotubular materials have attracted great attention because of their intrinsic multifunctionality, that arises from the distinct properties of different regions like as tube opening, inner, outer and interstitial regions.[2-4] Among such materials, TiO_2-based and titanate nanotubes, with typical dimensions less than 100 nm, are of great interest for photocatalysis, gas sensing, pigments, photovoltaic applications, solar cells and water detoxification because of their high surface area, porosity, low cost and chemical stability.[5-18]

In particular, titanate nanotubes combine the properties and applications of TiO_2 nanoparticles (eg., wide band gap semiconductor, photocatalyst) with the properties of layered titanates (eg., ion exchange) with tubular morphology.[9]

Titanate nanotubes are also of great interest for catalytic applications, since their high cation exchange capacity provides the possibility of achieving a high loading of metal cations via exchange procedures, which can be used to generate supported particles. In relation to this there are few demonstrated examples of successful utilization of titanate nanotubes as mesoporous catalyst supports for different nanoparticles: CdS decorated titanate nanotubes in reaction of photocatalytic oxidation of dyes,[10] ruthenium (III) hydrated oxide deposited on titanate nanotubes for selective oxidation of alcohols[14]. The nanotubular morphology of titanate could also be exploited in shape-selective catalysis.

To date, among the various techniques, the hydrothermal method consisting of treatment of TiO_2 with concentrated aqueous solution of NaOH, followed by a thorough acid washing, is fairly simple and enables the production of pure hydrogen titanate nanotubes at relatively low temperature.[9] Since then, the modification of titanate nanotubes by thermal treatments,[19-22] by adding functional groups[23] or by metal nanoparticles doping/loading[24,25] is becoming a challenging field. Owing to the heterogeneity of the obtained products in terms of structure and morphology of TiO_2, the role of the titanate structural motif in affecting the morphology of the resulting titania crystallites, has been highlighted .[21]

Despite a complete and reliable description of the crystal structure of titanate nanotubes is quite difficult due to the poor crystallinity, [26] it has been widely recognized that the titanate nanotubes formed via-proton ion-exchange route from exfoliated sheets of sodium titanates nanotubes, or alternatively from lamellar titanates can be described as orthorhombic lepidocrocite- type structures ($A_2Ti_2O_5 \cdot H_2O$, or $A_xTi_{2-x/4}\square_{x/4}O_4$, where A= Na^+ and/or H^+; $\square$ = vacancy).[26-30]. In other words, the building up of scrolled nanostructures was explained in terms of wrapping of the layered sodium titanates, which were formed during the preliminary alkaline hydrothermal treatment of the TiO_2 raw material. [31].

Due to the variety of the synthesis conditions (i.e. temperature and times of reaction, concentration of reagents, etc.), several products can be obtained. In particular, during the HCl treatment, sodium ions are usually replaced by protons at lower pH, giving rise to a variety of hydrogen containing titanium oxides, among whose: monoclinic trititanate ($H_2Ti_3O_7$)[32], orthorhombic $H_2Ti_2O_4(OH)_2$,[33] monoclinic $H_2Ti_4O_9 \cdot H_2O$,[34] lepidocrocite-type structures ($H_2Ti_2O_5 \cdot H_2O$),[30] and TiO_2 nanotubes,[19], which then decompose at high temperature calcinations.[9] All the proposed hydrogen containing structures have the following common properties: i) a well defined layered structure with a relatively large interlayer distance, ii) the presence of hydrogen cations inside the interlayer cavities, easily exchangeable with alkali metal ions, iii) the presence of edge-and corner sharing TiO_6 octahedra building up to zigzag structures.[9] Since titanate nanotubes have high specific surface area with nanoscale inner cavities, it is therefore of great interest to encapsulate or decorate them with noble nanoparticles, such as gold or

silver. Furthermore, the confinement and the template effects by the one-dimensional structure of the titanate nanotube, encapsulating silver clusters with controlled shape inside the inner cavity or in the interlayer spacings, can be highlighted as example of spatial nanometric structuring of metal particles inside a host framework. [35] In fact, cavities of limited size can effectively control agglomeration phenomena of nanoparticles,[36] a fact which can be beneficial for the induction of enhanced catalytic efficiency, surface plasmon absorption and non linear optical properties, all factors encouraging the fabrication of metal-loaded nanotube films for photocatalytic and photovoltaic applications.

It has been demonstrated that depending on the precursor, the layered protonated titanates could be directly transformed to anatase or can be first converted to the metastable monoclinic TiO_2 (TiO_2-B) and then to TiO_2 under calcinations. [9,26,37]

Nevertheless, as far as titanate-TiO_2 transformation is concerned, it is known that phase, size and dispersion of the obtained TiO_2 nano-crystallites are affected by addition of transition metal salts, whose role in affecting surface area, crystallinity, as well as photocatalytic activity is highlighted. [38-44] These results confirm that, for TiO_2 based catalysts, a higher crystallinity is relevant for an enhanced photocatalytic activity and the function of the transition metal is to increase the electron-hole recombination time, therefore the catalytic activity. [41]

The aim of the paper is to show that the nature of the raw materials, the alkaline hydrothermal conditions and then the thermal post-treatments, combined together with the metal doping/loading, affect the titanate structural motif and then the structure and the morphology of the resulting titania crystallites. The combined approach can produce a new generation of materials with high photocatalytic efficiency under visible and solar light, as shown by some relevant reports. [35,41,45]

Following this line, in this paper the synthesis, the structure and the properties of pure and silver loaded titanate nanotubes have been studied. The study is divided into two parts.

In the first one, we discuss the synthesis and the morphological transformations of titanate nanotubes, into anatase titania nanostructures, under relatively mild temperatures (500°C). It will be shown, that the transformation of titanate into titanium oxide leads to the formation of TiO_2 particles.

In the second part, silver loaded titanates and their transformation into anatase nanoparticles are investigated and the role of the silver, in affecting morphology, crystallinity and optical properties of the nanostructures, is then highlighted.

The relation between morphology and structure of the titanate precursor and of the formed TiO_2 particles (both pure or silver loaded) has been investigated by means of BET, powder XRD analyses, HRTEM, AFM and SEM microscopies. Surface and optical properties have been explored by means of FTIR and UV-vis diffuse reflectance spectroscopies.

2. Experimental

2.1 Synthesis

In a typical synthesis procedure, the preparation of the titanate samples is performed in several steps. First, the anatase powder (Aldrich anatase 99.8, 1,5 g, with sizes in the 50-250 nm range) has been treated with a NaOH solution (60 ml, 10M) inside a 125 ml PTFE High Pressure Reactor, then placed into an oven for 20 hours at 150 °C. The so obtained material, constituted by the sodium titanate phase, has been then treated in 0.1 M HCl solution for 5 hours at room temperature under stirring. Before and after the acid treatment, the samples have been washed/filtered several times and dried at 120 °C.

To study the hydrogen titanate-TiO_2 transformation, a portion of the hydrogen titanate powder has been thermally treated, in a quartz tube at 500 °C for 2h under 135 ml/min air flow, whereas, to study the effect of silver loading, the residual portion of the H-titanate powder, has been ion exchanged with a solution of $AgNO_3$ (0.01 M, 50% w/v) at 25 °C, for 20 hours, being 0,121 w/w the weight ratio of silver to titanate in the solution, before filtering, drying and calcining. Then the sample was thermally treated at 500°C in the same way.

2.2 Characterization techniques

The morphology of the samples has been investigated by means of SEM (Zeiss Evo50 equipped with an Oxford Energy Dispersive X-ray detector), TEM (JEOL 3010-UHR instrument operating at 300 kV, equipped with a 2k x 2k pixels Gatan US1000 CCD camera) and AFM (Park Scientific Instrument Auto Probe LS) microscopies.

The crystallinity of the samples has been estimated by XRD analysis (PANalytical X'Pert PRO diffractometer equipped with a Ni filtered Cu radiation in a standard Bragg–Brentano geometry). The crystallite size was calculated from XRD measurements by Scherrer's equation.

N_2 adsorption–desorption experiments have been carried out at 77 K (Micromeritics ASAP 2020 instrument) to determine the Brunauer–Emmett–Teller (BET) surface area; before the analysis the samples were outgassed at 150°C for 6 h. The t-plot method has been employed to qualitatively interpret the pore structure by analyzing the evolution of N_2 adsorption branch, while the Horvath-Kawazoe (HK) and the Barrett-Joyner-Halenda (BJH) models have been applied to the adsorption and to the desorption branches of the isotherms in the micro- and in the meso/macroporosity range, respectively.

Diffuse reflectance UV–vis spectra have been recorded directly on the materials at room temperature (300K) by means of a UV-Vis-NIR spectrometer, equipped with a diffuse reflectance attachment (Varian Cary UV 5000 UV-VIS-NIR) before and after irradiation with solar lamp (SOL2/500S) simulating solar light irradiation, ranging approximately in the 3000-295-nm interval.

All the samples have been pressed into self-supporting pellets and transferred to IR quartz cell, where they have been outgassed in vacuum at T = 423 K and 773 K for 2.5 h and then treated with oxygen ($p(O_2)$ = 5,33 kPa) at the same temperatures for 1.5 h in static conditions. The oxygen has been changed three times every 30 minutes. The outgassed samples, after cooling at 300K under oxygen, have been dosed with CO (p(CO) = 5,33 kPa) and FTIR spectra have been recorded at 77 K: then the pressure has been gradually reduced in steps. After each step, the FTIR spectrum of adsorbed CO species has been obtained. All FTIR measurements have been carried out in situ at 2 cm^{-1} resolution, using a Bruker IFS 28 spectrometer, equipped with a cryogenic MCT detector.

3. Results and Discussion

3.1 Morphology, structure and surface area of the materials

3.1.1 SEM characterization

The morphology of H-titanates and Ag-titanates, before and after thermal treatments, as obtained by SEM, is illustrated in Fig. 1a–d.

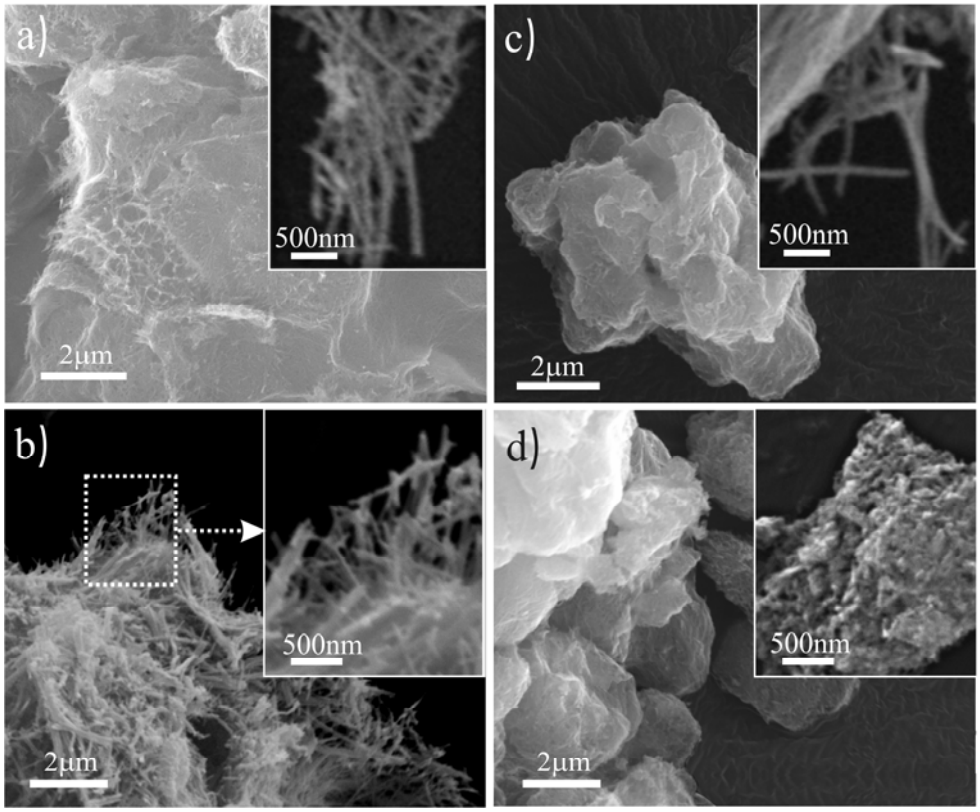

Figure 1. SEM images of hydrogen titanates (a) before and (b) after thermal treatment at 500 °C. SEM images of silver titanates (c) before and (d) after thermal treatment at 500 °C. Insets: enlarged views of agglomerates, taken in more external position.

The H-titanate sample (Fig.1a, and inset therein) is constituted by dense bundles of elongated titanate nanostructures with diameter in the 40÷100 nm and lengths in the 1÷2 μm ranges, at the adopted resolution (inset of Fig. 1a), which are comparable with the crystal sizes of the starting anatase material (not shown for sake of brevity). From this figure, the formation of a fibrous nanostructured material, having nanofilaments protruding at the borders, is observed.

After the thermal treatment, (Fig.1b and inset therein), agglomerates of thicker and less elongated nanostructures, 50÷200 nm wide and 100÷500 nm long, are observed, which are formed via the partial breaking of the filaments.

The Ag ion-exchanged sample (≈ 6% wt/wt Ag, estimated by EDAX analysis, after filtering, drying and before calcination) (Fig.1c and inset therein) appears as a more compact material, also constituted by aggregates of bundles, whose diameters and lengths are comprised in the 50÷150 nm and in the 2÷5 μm ranges, respectively. Upon the thermal treatment (route 2), the silver containing samples (≈ 8% wt/wt Ag, estimated by EDAX analysis, after calcination) undergo remarkable morphology changes, as evidenced in Fig.1d. From this figure, the disappearance of elongated nanostructures is emerging. In particular, bundles of very short fragments, 100÷200 nm in length and agglomerates of nanoparticles, with dimensions ranging in the 50÷200 nm interval are formed (inset of Fig. 1d).

From these figures, we can conclude that the thermal treatments are affecting the morphology of the starting samples, giving rise to fragmented nanostructures, being this effect more evident for silver loaded samples. These results are confirmed by BET analysis of the surface area (*vide infra*).

3.1.2 TEM, AFM, HRTEM and XRD analyses

As far as the structure, at the nanometer scale, of the original bundles and of the fragments obtained upon thermal treatments, TEM analysis is more informative.

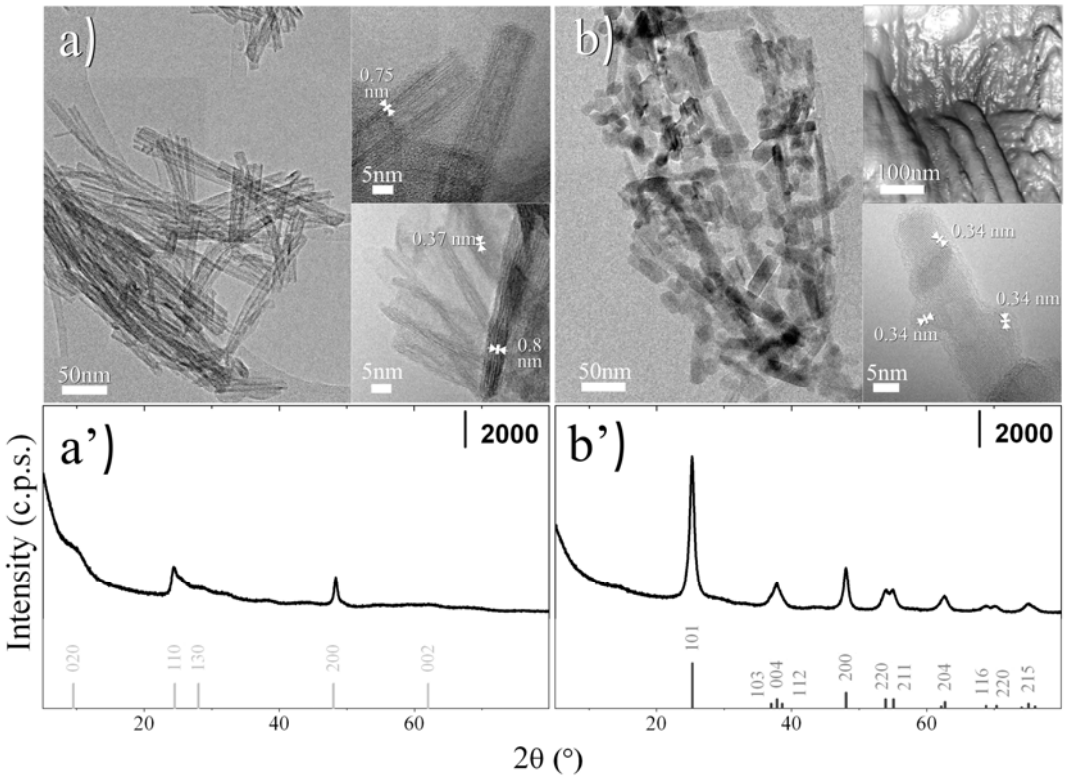

Figure 2. (a) TEM images of hydrogen titanates before thermal treatment at 500 °C. In the insets are HRTEM images of a few nanotubes. (a′) XRD pattern of the hydrogen titanate nanotubes, as compared to the reference XRD pattern of the orthorhombic lepidocrocite-type titanates.[30,46] (b) TEM images of hydrogen titanates after thermal treatment at 500 °C. Insets: (on the top) AFM images of nanofilaments, about 50 nm in diameter (as obtained from the height profiles, not reported for the sake of brevity) and trapped in a more heterogeneous network; (on the bottom) nanocrystals anchoring or overlapping on a more elongated single nanofilament. (b′) XRD pattern of the TiO_2 nanoparticles, as compared to the reference XRD pattern of the standard anatase.

In particular, from Fig. 2a (and inset therein) it is clearly evidenced that the elongated nanostructures, already observed in Fig. 1a, are constituted by well shaped nanotubes (10÷20 nm in diameter, with internal cavities about 5 nm in size and 200÷300 nm in length). From a more accurate investigation, the nanotube walls (top and bottom right inserts) appear to be constituted by a few layers (0.75÷0.8 nm spaced), which are surrounding the nanotube internal cavity and by a second family of planes (0.36÷0.37 nm spaced) (bottom insert), which are running perpendicularly to the previous ones. They correspond respectively to the (020) and to the (110) crystalline planes of the orthorhombic

lepidocrocite-type titanate structure.[30,46] This is confirmed by XRD pattern in Fig. 2a', where the H titanate phase shows two main narrow peaks (at 2θ ≈ 24,3° and 48,3°) and minor broad features at 2θ ≈ 10° and at 28,5°, which can be readily assigned to the (110), (200) and (020), (130) diffraction planes of the orthorhombic-lepidocrocite-type titanate,[21,30,46,47] being the (020) ones associated with the interlayer distance of the as prepared nanotubes.

After thermal treatment at T = 500 °C, the nanotubes partially break and the hollow cavities disappear, as clearly shown in Fig. 2b. This is in agreement with the reported data concerning the conversion of the protonated titanates into the anatase phase by thermal dehydratation,[9,21] which is associated with the collapse of the interlayer spacing between the walls of the nanotube, resulting in domains of anatase phase.[48]

The progressive evolution of the elongated nanocrystals into more isotropic structures, having well defined morphology, can be confirmed from the AFM and HRTEM results imaged in Fig.2b (top and bottom right inserts, respectively). As matter of fact from AFM image (top right insert), nanofilaments, about 50 nm in diameter, (as obtained from the height profiles, not reported from sake of brevity) and trapped in a more heterogeneous network are observed.

The nanofilaments show, along and perpendicularly to their structure, small and regular features, which are due to fragmentation processes. Furthermore, the HRTEM image (bottom right insert) clearly shows the presence of chains of TiO_2 nanocrystals, which are reminescent of the original nanotubes organizations.

Their crystalline nature is testified by the observation of interference fringes 0.34 nm spaced and corresponding to the anatase (101) crystalline planes. In conclusion, it is confirmed that in this condition the titanate phase is quite completely converted into anatase TiO_2. The collapse of the fibrous structure is also confirmed by XRD results, as reported in Fig. 2b', where several peaks at 2θ ≈ 25,2°, 29,7°, 48,1°, 54°, 55°, 62,7°, 68,9°, 70,1° and 75,1°, corresponding to the (101), (004), (200), (105), (211), (204), (116), (220) and (215) crystalline planes of the anatase phase, are evidenced.

From the peak broadening and by using the Scherrer's equation ($d = K\lambda/(\beta\cos\theta)$, where d is the mean crystal size, λ is the X-ray wavelength, β is the FWHM of the diffraction line, corrected by the instrumental broadening, θ means the diffraction angle and K is a constant, which has been assumed to be 0.9, scattering coherent domains of ≈ 11 nm have been calculated along the (101) anatase plane direction.

TEM images of Ag-loaded nanostructures, obtained after calcination at 120 °C, are shown in Fig. 3a and b.

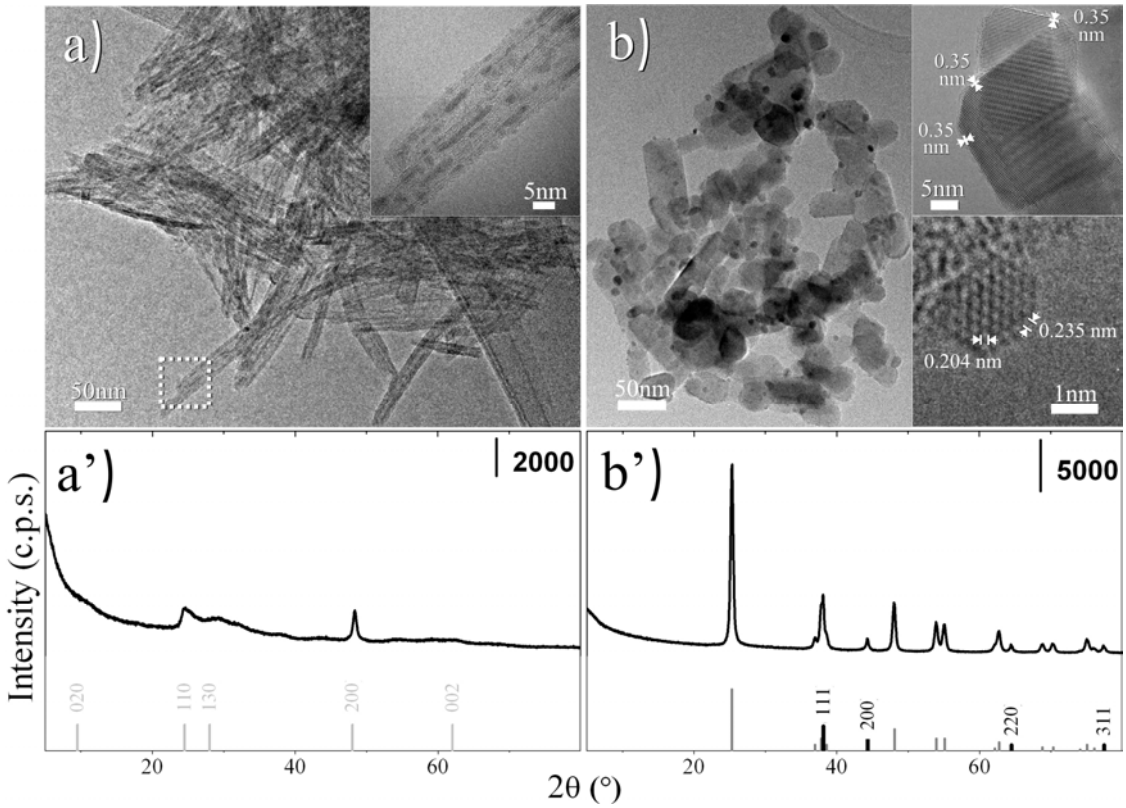

Figure 3. (a) TEM images of silver titanates before thermal treatment at 500 °C. (Inset) HRTEM image of two close nanotubes, where silver clusters are partially filling the cavities of the hollow nanofilaments. (a′) XRD pattern of the Ag-titanate nanotubes, as compared to the reference XRD pattern of the orthorhombic lepidocrocite-type titanates.[30,46] (b) TEM image of silver titanates after thermal treatment at 500 °C. Insets: (on the top) HRTEM image of a couple of well-defined and regular TiO2 nanocrystals; (on the bottom) HRTEM image of a highly defined and regular silver nanocrystal. (b′) XRD pattern of the thermally treated Ag -titanates, as compared to the anatase (gray lines) and to the fcc Ag (black lines) reference XRD patterns.

A network of elongated nanostructures having dimensions similar to those of pure samples is clearly evidenced. From the enlarged view image (top right insert in fig.3a) the presence of silver clusters, of variable shape and dimensions and filling the cavities of the hollow nanofilaments, is revealed. Upon thermal treatment at 500 °C (Fig. 3b) the structure changes in a remarkable way from a complex envelope of bundles to a rather homogeneous collection of well defined and regular anatase nanoparticles (20 ÷100 nm in size), supporting a wide distribution of silver particles (*vide infra*). More in detail, in the top right insert of Fig.3b, a highly regular and crystalline particle is HRTEM imaged, with two intercrossing families of interference fringes, 0.35 nm spaced, and corresponding to (101) anatase TiO_2 planes. These planes give rise to the [111] zone axis, which, together with the [100] zone axis, calculated on other HRTEM images (not reported for sake of brevity), represent the main orientations of the anatase particles. Besides, well defined silver particles, with diameter in the 1÷10 nm range, are observed on the highly regular anatase nanocrystals (Fig.3b, bottom right insert). From the evaluation of the interference fringes 0.24 nm and 0.20 spaced, corresponding to (1-11) and (002) crystalline planes, the [110] zone axis of fcc Ag was found. This feature confirms the crystalline nature of every single silver nanoparticle.

The XRD patterns of the Ag-titanate sample (before and after calcination at 500°C) are shown in Fig. 3a' and 3b'. Curve 3a'exhibits two main narrow peaks at $2\theta \approx 24{,}2°$ and 48,3° and minor broad features at $2\theta \approx 11{,}1°$ and 29,1°, which have been assigned to the (100), (200), (020) and (130) diffraction

planes of the lepidocrocite-type titanate structure.[46] Moreover curve 3b', beside the typical features at 2θ ≅ 25,2°, 37,0°, 37,8° (shoulder), 48,1°, 54°, 55°, associated with the (101), (103), (004), (200), (105) and (211) XRD diffraction planes of the anatase phase, exhibits new features at 2θ ≈ 38,1°, 44,3° and 64,4°, which are related to the (111), (200) and (220) diffraction planes of the metal silver cubic structure.

From the peak broadening and by using the Scherrer's equation, scattering coherent domains of ≈ 22 nm and ≈ 25 nm, respectively, have been calculated along the (101) plane direction of the anatase and along the (111) diffraction plane of the Ag phase. This suggests that silver nanoparticles are mainly coating the TiO_2 nanocrystals, even if from HRTEM images the presence of smaller encapsulated silver clusters cannot be excluded.

Finally, by comparing the weak envelope at 2θ ≈ 36÷39° in Fig. 3a' with the peak observed at similar diffraction angles in Fig. 3b', we can state that on silver loaded sample, a more resolved feature can be observed, which is splitting into two components at 2θ ≈ 37,0°, 38,6° (shoulder), assigned to the (103) and (112) diffraction planes of the anatase and one feature at 38,1° due to the (111) crystalline planes of the metal silver. In general, on silver loaded sample all the peaks are better defined and narrow (fig.3b'). This result can be explained in terms of high cristallinity and it is in agreement with the results obtained by HRTEM.

This means that the presence of silver nanocrystals plays a role in: i) reducing the surface area and ii) enhancing the crystallinity degree of the TiO_2 nanoparticles. A possible explanation concerning the role of Ag^+ in enhancing the crystallinity of the sample can be found in its activity in promoting the suppression of the formation of Ti^{3+} species. [49] It was reported that Ag^+ are reduced and segregated from the anatase TiO_2 matrix. Thus, during the calcination, there is a competition between the reduction of Ti^{4+} and Ag^+ ions, where the later reaction prevails because of its higher potential for reduction. The formation of Ti^{3+} species does not proceed and the product after calcination could be a material composed by silver clusters dispersed in the anatase TiO_2 matrix, that presents less defects than the pure anatase oxide, obtained in the same conditions. This explanation is in agreement with the results of other authors, [40] that correlate the reduction of intrinsic defectivity with the photoactivity improvement.

Coming back to the aforementioned top right inserts in Fig. 2a and Fig.3a, now reported as enlarged views (Fig. 4a,b), more considerations have to be made.

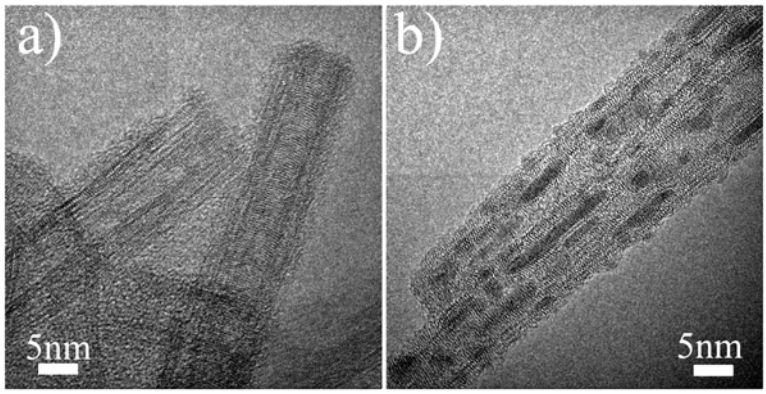

Figure 4. Enlarged view of HRTEM images of (a) hydrogen titanates and (b) silver titanates, both before thermal treatment at 500 °C.

In particular, the building up of hollow hydrogen titanate nanotubes (Fig.4a), coming from sodium titanates nanotubes, less than 10 nm in diameters (HRTEM images, not reported for sake of brevity) is highlighted. Besides, the occurrence of a different number of external layers on either side, surrounding the hollow cavity, is indicating, in agreement with literature data, that the multiwalled nanotubes are actually coming from the scrolling of layered nanosheets.[50]

Moving to the Fig.4b, the elongated shape of the encapsulated nanoparticles reflects the confinement and the template effects by the one-dimensional structure of the nanotube, being these effects due to either the inner cavity or the interlayer spacing, as evidenced from HRTEM image (Fig.4b). This is in agreement with the hypothesis that their stability probably arises from strong interactions between the silver clusters and the surrounding oxygen atoms of the nanotube.[36]

These silver clusters are not present in the sample before TEM analysis: so they are the result of the electron beam irradiation (Fig. 4b). This is further testified by the absence of Ag° clusters on the XRD pattern of the Ag-titanate samples, by the reflectance spectra (the samples are white, while Ag° clusters are coloured) and by the appearance of the IR bands associated to CO adducts on Ag charged species ($Ag_n^{\delta+}$ ····CO adducts) (*vide infra*).

3.1.3 Surface area and porosity

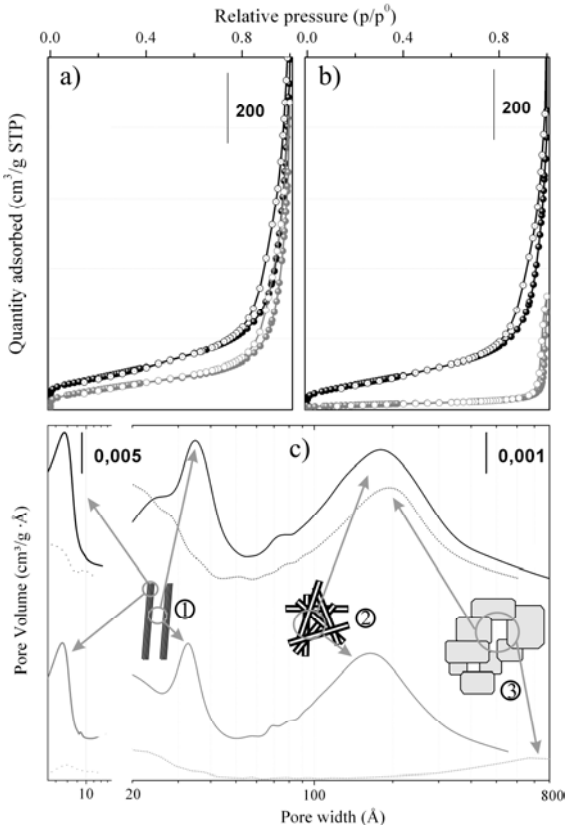

Figure 5. N_2 adsorption/desorption curves of (a) hydrogen titanate nanotubes before (black curves) and after thermal treatment (gray curves); (b) Ag-titanates before (black curves) and after thermal treatment (gray curves); (c) pore size distributions of hydrogen titanates (black line), of Ag titanates (gray line), and of the same samples after thermal treatment at 500 °C (black and gray dotted lines), as obtained from HK and BJH models in the micro- and in the mesoporosity ranges, respectively. Schemes inside the figure correspond respectively to (1) the nanotubes structures, (2) the voids due to nanotubes aggregation processes, and (3) the macropores within TiO_2 nanoparticles.

The N_2-adsorption/desorption isotherms of the samples, obtained on hydrogen and silver titanates dried at 120 °C (black curves) and thermally treated at 500°C in air (gray curves), are shown in Fig.5a,b.

Both the hydrogen and silver titanate isotherms, treated at 120 °C (Fig. 5a,b), exhibit a pronounced hysteresis loop, indicating the presence of mesopores related to the prevalent contribution of the nanotube cavities, while the weak hysteresis loop observed on the thermally treated samples (gray curves) can be explained with a porosity coming from the aggregation state of the TiO_2 nanoparticles.[51] The simultaneous downshifting of the isotherm plateaus (Fig.5a,b) means that, after thermal treatments, the specific surface area (s.s.a.) is decreasing (see Table 1).

Although similar features can be observed on both samples, more pronounced effects are evidenced on the silver loaded sample treated at 500 °C. As a matter of fact, in this case, the surface area declines abruptly to 51 m^2g^{-1} and the hysteresis loop is much more constrained, as compared to that of the pure sample, treated at the same temperature.

Table 1. BET surface area and porosity properties of the samples.

	BET Surface Area (m^2/g)	Micropore Area [i] (cm^2/g)	Mesopore Area [ii] (cm^2/g)	Total pore volume[iii] (cm^3/g)	Limiting micropore volume[iv] (cm^3/g)
Protonated titanate	328	-	299	1.05	0.11
Ag-titanate	267	-	249	0.819	0.09
TiO_2	216	-	186	0.757	0.06
Ag-TiO_2	51	-	42	0.103	0.02

[i] Estimated by using t-plot method, (Harkins and Jura thickness curve),

[ii] Estimated by using the BJH adsorption branch of the isoterms,

[iii] Single-point total pore volume at $P/P_0 \cong 0.97$,

[iv] obtained by Dubinin-Astakhov model

The decrement of surface area upon thermal treatments at 500°C is associated with the disappearance of the nanotube structure on both materials. This hypothesis is confirmed by the pore size distributions (PSDs), as obtained in the microporosity range (Fig. 5c, left side) by the Horvath-Kawazoe (HK) equation and in the meso/macroporosity range (Fig. 5c, right side) by the Barrett-Joyner-Halenda (BJH) model, applied to the adsorption and the desorption branches of the isoterms, respectively.

From this figure, the hydrogen titanate PSD (curve 1) shows a monomodal distribution in the 6.5÷8.5 Å range with a maximum at ≈ 8 Å (very sharp) and a bimodal distribution in the 20÷500 Å range, with maxima at ≈ 35 Å (sharp) and at ≈ 181 Å (broad), while the PSD of the thermally treated sample (curve 2) exhibits two broad bands, in the ≈ 6÷9 Å and in the 70÷500 Å ranges with a maximum at ≈ 194 Å and a tail that decreases in the 20÷40 Å range. The maximum of the sharp monomodal distribution centred at ≈ 8 Å (curve 1) is very close to the (020) interplanar distance of the nanotube scrolled multilayers, as obtained from XRD (≈ 8.6 Å) and TEM (≈ 8 Å) analyses (scheme in the figure). The sharp and the broad bands, in the mesoporosity range (maxima at ≈ 35 Å and at ≈ 181 Å) are thought to correspond, respectively, to the inner diameter of the nanotubes and to the voids caused by nanotubes aggregation processes (see schemes inside the figure).[51] The same can be inferred by comparing the PSDs of the silver loaded samples before and after the thermal treatment at 500°C (curve 3 and 4, respectively). As a matter of fact, curve 3 shows a monomodal distribution in the 6÷8 Å range with a maximum at ≈ 7.5 Å (very sharp) and a bimodal distribution, in the 25÷400 Å range, with maxima at ≈ 33 Å (sharp) and ≈ 164 Å (broad), while curve 4 shows a weak and wide band in the 350÷800 Å range

with a maximum at ≈ 750 Å, which is mainly ascribed to the presence of macropores coming from the aggregation of larger TiO_2 nanoparticles (scheme in the figure).

3.2 Optical properties

Fig. 6 shows the diffuse reflectance UV-vis spectra of the hydrogen titanates, as prepared and after thermal treatment, both pure and silver loaded, together with the anatase precursor, as reference spectra. The band edge energies, [41,52] due to the transition from $O^{=}$ antibonding orbital to the lowest energy orbital of Ti^{4+}, have been evaluated by plotting $(\alpha E)^{1/2}$ (where α and E represent the absorption coefficient and energy, respectively) against the incident photon energy ($h\nu$) (data not reported for sake of brevity).

In particular, the spectrum of the hydrogen titanate sample exhibits an adsorption edge at ≈ 374 nm, which is slightly downward shifted to ≈ 380 nm after thermal treatment at 500 °C. The same behavior can be observed for silver loaded samples. Similarly, the adsorption edge of the silver titanates, placed at ≈ 375 nm, shifts to ≈ 385 nm after the thermal treatment, thus confirming significant structure changes, in agreement with BET surface area.

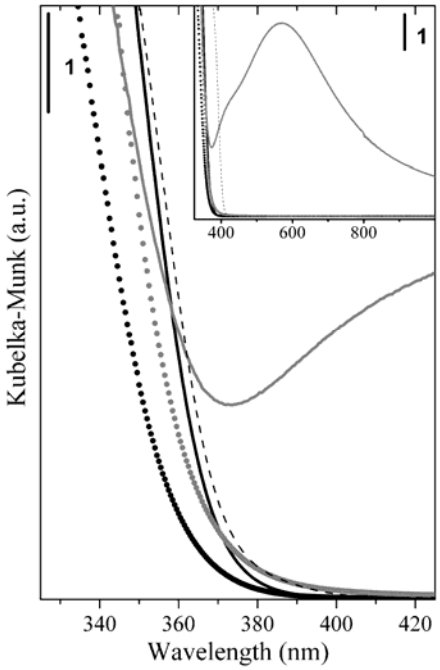

Figure 6. UV-visible spectra of hydrogen titanate before (black dotted curve) and after thermal treatment at 500 °C (black solid lines), Ag titanate nanotubes before (gray dotted curve) and after thermal treatment at 500 °C (gray solid curves), and anatase (- - -). Inset: surface plasmon resonance absorption of Ag-titanates after thermal treatment at 500 °C.

It is noteworthy, that nanostructured TiO_2 samples (either pure or silver loaded) obtained after calcination at 500 °C, show an absorption edge, slightly upward shifted with respect to that of pure TiO_2 (anatase precursor). The observed small blue shift is due to quantum size effects, characteristic of typical small particles, which is known to increase the band gap with respect to that of infinite crystals.[21] This means that the conversion to anatase phases, promoted by the thermal treatments, leads

to the formation of TiO_2 crystallites, whose size is smaller than those of the precursor anatase and of P25 (TEM and XRD data not reported for sake of brevity).

Coming back to the TiO_2-titanate transformation, as discussed by many authors,[21,24,28,30] a reduction of dimensionality, by moving from 3D to 2D up to 1D, results in a change of physical-chemical properties e.g. appearance of new optical bands and crystal structure changes. Along this theme, it was shown that the band gap of TiO_2 nanosheets is strongly blue shifted relative to the band gap of bulk TiO_2 , due to the lower dimensionality, i.e., a 3-D to 2-D transition. Similarly TiO_2 nanosheets transformation to TiO_2 nanotubes is resulting in addition loss of dimensionality i.e., a 2-D to 1-D transformation. [21] In our opinion, for our systems, the observed frequency shifts, although very low, can be correlated with the topotactic transformation of titanate nanotubes into TiO_2 (plausibly from a 1-D to 3-D transformation).

With regard to the metal loading effect on the absorption spectra, a red shift for silver loaded titanates nanotubes with respect to hydrogen titanates was observed. This could be related to the ion exchange process, promoted by Ag^+, which favors the partial swelling of the outermost layers to occur. These data are in agreement with some reports, which show that the frequency shift of quasi-2D crystallites is governed predominantly by their layer thickness.[30]

Nevertheless, although the results, concerning the effect of various metals on the band gaps, are often controversial, [53] a significant correlation between the metal concentration and the photoactivity of the resulting metal-loaded catalyst is widely proved. [35,41,45] More in detail, it comes that the photoactivity of TiO_2-based materials generally increases, with increasing the concentration of metal loading, reaches a maximum value and afterwards decreases. [53] According to some authors the photocatalytic activity of transition metal loaded TiO_2 was determined at least by two parameters: the amount of metal and the active sites of the TiO_2, the second ones being related to surface area. [41] In particular, for Ag/TiO_2 systems, a higher activity was obtained by 0.1 mole ratio of metal to TiO_2, corresponding to 11,9 % wt of silver. [41] The role of silver loading was also highlighted by other reports, where the photodegradation activity of silver modified TiO_2 catalysts (with 0.5, 2.0 and 5.0 wt % of Ag) has been discussed. From these results, it comes that the samples containing the higher amount of silver are more active. [49]

On the basis of these data, we expect that the silver loaded samples, obtained in this work (8% w/w Ag, estimated by EDAX analysis, after calcination) can reasonably show rather high activities**.**

It is worthy noticing that, on silver titanate thermally treated at 500°C, a broad and intense absorption band in the 400÷950 nm range with a maximum at ≈ 570 nm is also observed (inset in Fig.6), which is explained with surface plasmon resonance (SPR) effects due to Ag nanoparticles.[54,55]

It is known, that many factors, like symmetry, shape, size, imbedding medium and interaction between nanoparticles are affecting the position and the shape of the plasmon absorptions.[55]

To this regard, because of the wide amplitude and the significant broadening of the absorption, extending from 400 to 850 nm, due to the excitation of higher plasmon modes,[56] a large size distribution of silver particles is expected, with diameters ranging from 2 nm (as shown from HRTEM image of Fig. 3b) up to the much larger values of clusters ≈ 25-50 nm in size. Their anisotropic shapes, together with an advanced stage of aggregation are consistent with the TEM and XRD results, previously discussed and with the published results for supported silver particles.[15] In general, red shift and increase in the surface plasmon band with increasing particle size were observed for nanoparticles supported on solid surfaces.[57,58]

Moving to Fig. 7, the diffuse reflectance UV-visible spectra of silver loaded titanates, before and after solar irradiation are shown.

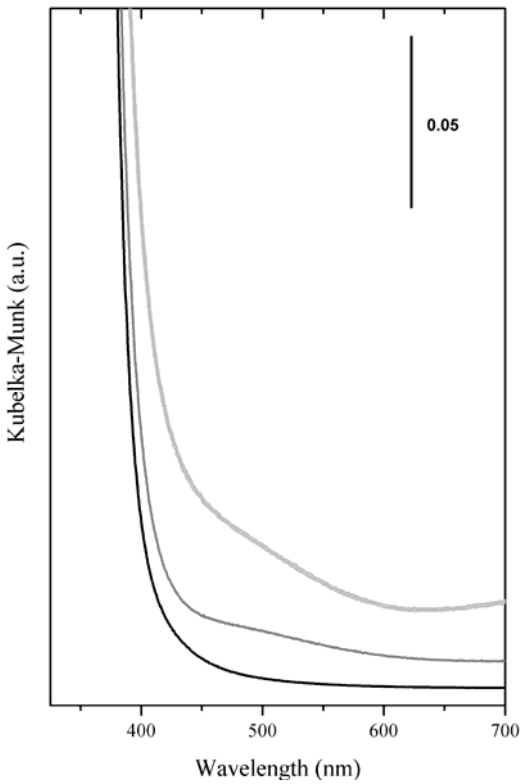

Figure 7. UV-visible spectra of silver titanate before (black curve) and after solar light irradiation under 250 W (dark gray curve) and 900 W (light gray curve), respectively.

The absorption edge of silver loaded titanates at 375 nm (black curve) is slightly downward shifted to ~ 425 nm (dark gray curve) and ~ 450 nm (light gray curve) after irradiation at different power (250W and 900W, respectively), while a broad and weak absorption band is simultaneously observed in the 450-550 nm range. It is worthy noticing that these features are less intense than those observed on silver titanates, thermally treated at 500 °C.

A further confirmation to these data comes from a published report,[44] where a relevant photochromic behaviour has been observed on silver titanates samples exposed to monochromatic radiations at different wavelengths (640, 580, 520, 450 and 405 nm). Similarly, a relation between the photochromic behavior and the formation of metal silver particle with different sizes has been found.[44]

3.3 Vibrational properties

The FTIR spectra of CO adsorbed at 77 K, at decreasing coverages, on the surface of titanate phases (activated at 150 °C to eliminate adsorbed water) and on TiO_2 surfaces (outgassed at 500 °C), both pure or silver loaded, are reported in Fig. 8a-d.

The titanate sample outgassed at 150 °C in vacuum is entirely hydroxylated, as shown in the insert of Fig. 8a, where intense and broad bands in the OH region are observed. From this we can state that the peak at 2156 cm^{-1}, slightly downward shifting with the coverage to 2152 cm^{-1}, is due to -OH····CO complexes on the (020) and/or (110) crystalline planes of the multiwalled titanate nanotubes, in agreement with the literature data.[48]

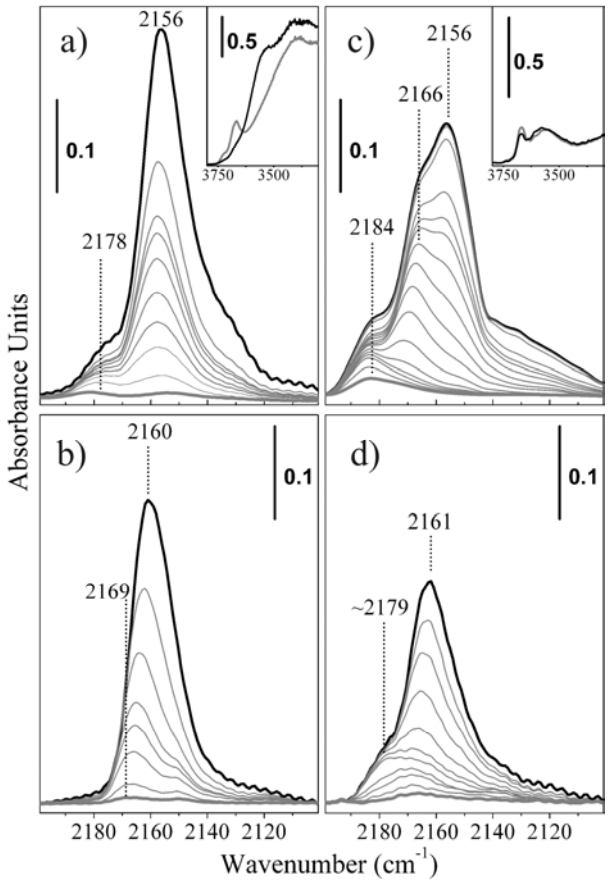

Figure 8. FTIR spectra of CO adsorbed at 100 K at increasing coverages on hydrogen titanates (a) before and (b) after thermal treatment at 500 °C; (c) Ag-titanates before and (d) after thermal treatment at 500 °C (bold black spectra: pCO) 10 mbar, bold gray spectrum: pCO) 0 mbar, gray spectra: 0 < pCO < 10 mbar). The insets report the same spectra in the 3750-3300 cm^{-1} region.

The presence of a shoulder at 2178 cm^{-1}, is plausibly due to Na^+ ····CO complexes formed on residual Na^+ ions. [59,60]

As far as the weak shoulder at 2130-2135 cm^{-1}, it vanishes after short evacuation, which confirms its assignment to physically adsorbed CO.[61]

The spectra of CO adsorbed on the sample calcined and outgassed at 500 °C (partially dehydroxylated sample) are reported in Fig. 8b. The dominant peak at 2160 cm^{-1} is assigned to the mode of parallely arranged CO oscillators adsorbed on five-fold coordinated Ti^{4+} sites on the main exposed TiO_2 surfaces. From this figure, it can be observed that, by decreasing the CO coverage, the peak gradually shifts from 2160 cm^{-1} to 2169 cm^{-1}. This effect can be explained as the progressive vanishing of the dynamic and static lateral interactions among the CO oscillators. The final frequency (2169 cm^{-1}) is associated with isolated Ti^{4+}····CO species.

This assignment is in agreement with previous reports, [61,62] where the peak in the 2160-2169 cm^{-1} range has been assigned to CO adsorbed at 100K on cus (coordinatively unsaturated) Ti^{4+} sites (g sites) on (001) faces, possessing a very low electrophilicity, and on some edges such as (101)x(011). The absence of the typical features at 2206 cm^{-1} and 2175 cm^{-1} associated with CO adsorbed on highly electrophilic Ti^{4+}_{4c} and Ti^{4+}_{5c} species (referred to α and β sites respectively on (110) and (100), (101) planes) can be justified in terms of the peculiar morphology, shown by the TiO_2 crystallites (Fig.2b). [56,62,63] However, the contribution of the stretching mode of CO oscillators adsorbed on the residual Na^+

species, remaining on the sample after hydrogen exchange (≈ 0.8 % w/w Na, estimated by EDAX analysis) cannot be ruled out.

More complex features are observed on silver loaded systems, activated at 150 °C (Fig. 8c). In particular, beside the quite intense band at 2156 cm^{-1}, due to the presence of hydroxyls, an intense peak at 2166 cm^{-1}, shifting to 2171 cm^{-1} and a strong shoulder at higher frequency (2184 cm^{-1}) can be distinguished. The features in the 2166-2190 cm^{-1} region can be assigned to a variety of $Ag_n^{\delta+}$ ····CO adducts, uniformly distributed inside and on the external layers surrounding the nanotube cavity. Notice that the 2184 cm^{-1} high frequency peak has been observed on Ag^+ ZSM5, in the same frequency range, which has been assigned to $Ag^+(CO)$ and $Ag^+(CO)_2$ adducts. [64]

On silver doped samples, outgassed at 500°C (Fig.8d), the feature at ν ≈ 2166-2190 cm^{-1}, ascribed to Ag^+ (CO) species, is eroded. This result is in agreement with the HRTEM results, which show that the thermal treatment at 500°C favors the formation of silver particles. On this sample the main peak at 2161 cm^{-1}, shifting to 2169 cm^{-1} is the main feature of the spectrum. This peak is assigned to Ti^{4+}_{5c}····CO species on extended (001) surfaces of TiO_2 anatase. A further component at ν ≈ 2179-2180 cm^{-1} is also observed at high coverages, which can be assigned to a few $Ag_n^{\delta+}$ ····CO adducts, formed upon CO interaction on residual Ag^+ species, which have not been reduced to Ag° during the thermal treatment.

4. Conclusions

The transformation of high surface area titanate nanotubes, either in the hydrogen and in the silver exchanged form, into TiO_2 nanocrystals has been studied by means of SEM, TEM, AFM and BET methods. The thermal treatment at 500°C of hydrogen titanate nanotubes leads to the formation of quite regularly arranged crystalline TiO_2 anatase nanocrystals, coming from the fragmentation of the nanotubes. Thermal annealing leaves to densely spaced, regular holes inside TiO_2 nanocrystals, having higher surface area as compared with the commercial titanium oxide precursors.

On silver loaded titanates, the presence of Ag^+ species, converting to Ag^0 upon thermal treatment, plays a key role in promoting the formation of anatase nanocrystals. The so formed TiO_2 nanocrystals have reduced surface area, enhanced crystallinity and lower porosity, with respect to TiO_2 nanocrystals coming from hydrogen titanate nanotubes. The formation of silver particles supported on TiO_2 is fully demonstrated by HRTEM and UV-vis spectroscopy. For the first time, the surface properties of silver exchanged titanates, as compared with silver loaded TiO_2, have been investigated by FTIR spectroscopy of adsorbed CO. On silver exchanged titanates, the formation of $Ag^+(CO)_n$ (n =1,2) species has been revealed.

Finally, all the materials (as prepared, either in the hydrogen and in the silver exchanged form and those obtained after thermal treatments) show better performance than the commercial TiO_2 precursor and in general than those obtained by solid state reactions (P25), in terms of specific surface area and porosity.

In conclusion, we have shown that by adopting suitable raw materials, hydrothermal conditions and then thermal post-treatments, combined together with metal doping/loading, the titanate structural motif and then the structure and morphology of the resulting titania crystallites can be effectively tailored.

ACKNOWLEDGMENTS The authors would like to thank MIUR, INSTM Consorzio, NANOMAT Project for their financial supports and a special thank to Dr. Diego Pellerej for the technical support.

REFERENCES

(1) Iijima, S. *Nature* **1991**, *354*, 56.

(2) Hu, X. G.; Dong, S. J. *Journal of Materials Chemistry* **2008**, *18*, 1279.

(3) Rao, C. N. R.; Vivekchand, S. R. C.; Biswasa, K.; Govindaraja, A. *Dalton Transactions* **2007**, 3728.

(4) Tenne, R. *Nature Nanotechnology* **2006**, *1*, 103.

(5) Chen, X.; Mao, S. S. *Chemical Reviews* **2007**, *107*, 2891.

(6) Kamat, P. V. *Journal of Physical Chemistry C* **2007**, *111*, 2834.

(7) Cesano, F.; Bertarione, S.; Damin, A.; Agostini, G.; Usseglio, S.; Vitillo, J. G.; Lamberti, C.; Spoto, G.; Scarano, D.; Zecchina, A. *Advanced Materials* **2008**, *20*, 3342.

(8) Kongkanand, A.; Tvrdy, K.; Takechi, K.; Kuno, M.; Kamat, P. V. *Journal of the American Chemical Society* **2008**, *130*, 4007.

(9) Bavykin, D. V.; Friedrich, J. M.; Walsh, F. C. *Advanced Materials* **2006**, *18*, 2807.

(10) Xiao, M. W.; Wang, L. S.; Wu, Y. D.; Huang, X. J.; Dang, Z. *Nanotechnology* **2008**, *19*.

(11) Wang, M.; Guo, D. J.; Li, H. L. *Journal of Solid State Chemistry* **2005**, *178*, 1996.

(12) Rodriguez, J. A.; Ma, S.; Liu, P.; Hrbek, J.; Evans, J.; Perez, M. *Science* **2007**, *318*, 1757.

(13) Qu, J. P.; Zhang, X. G.; Wang, Y. G.; Xie, C. X. *Electrochimica Acta* **2005**, *50*, 3576.

(14) Bavykin, D. V.; Lapkin, A. A.; Plucinski, P. K.; Friedrich, J. M.; Walsh, F. C. *Journal of Catalysis* **2005**, *235*, 10.

(15) Uddin, M. J.; Cesano, F.; Bertarione, S.; Bonino, F.; Bordiga, S.; Scarano, D.; Zecchina, A. *Journal of Photochemistry and Photobiology a-Chemistry* **2008**, *196*, 165.

(16) Kasuga, T.; Hiramatsu, M.; Hoson, A.; Sekino, T.; Niihara, K. *Langmuir* **1998**, *14*, 3160.

(17) Papa, A. L.; Millot, N.; Saviot, L.; Chassagnon, R.; Heintz, O. *Journal of Physical Chemistry C* **2009**, *113*, 12682.

(18) Zhang, Y. H.; Ebbinghaus, S. G.; Weidenkaff, A.; Kurz, T.; von Nidda, H. A. K.; Klar, P. J.; Gungerich, M.; Reller, A. *Chemistry of Materials* **2003**, *15*, 4028.

(19) Mogilevsky, G.; Chen, Q.; Kulkarni, H.; Kleinhammes, A.; Mullins, W. M.; Wu, Y. *Journal of Physical Chemistry C* **2008**, *112*, 3239.

(20) Paek, M. J.; Ha, H. W.; Kim, T. W.; Moon, S. J.; Baeg, J. O.; Choy, J. H.; Hwang, S. J. *Journal of Physical Chemistry C* **2008**, *112*, 15966.

(21) Mao, Y. B.; Wong, S. S. *Journal of the American Chemical Society* **2006**, *128*, 8217.

(22) Mao, Y.; Kanungo, M.; Hemraj-Benny, T.; Wong, S. S. *The Journal of Physical Chemistry B* **2006**, *110*, 702.

(23) Shi, Z. Q.; Gao, X. P.; Song, D. Y.; Zhou, Y. F.; Yan, D. Y. *Polymer* **2007**, *48*, 7516.

(24) Bavykin, D. V.; Lapkin, A. A.; Plucinski, P. K.; Torrente-Murciano, L.; Friedrich, J. M.; Walsh, F. C. *Topics in Catalysis* **2006**, *39*, 151.

(25) Zhu, B. L.; Sui, Z. M.; Wang, S. R.; Chen, X.; Zhang, S. M.; Wu, S. H.; Huang, W. P. *Materials Research Bulletin* **2006**, *41*, 1097.

(26) Gao, T.; Fjellvag, H.; Norby, P. *Inorganic Chemistry* **2009**, *48*, 1423.

(27) Tsai, C. C.; Teng, H. S. *Chemistry of Materials* **2006**, *18*, 367.

(28) Lin, C. H.; Chien, S. H.; Chao, J. H.; Sheu, C. Y.; Cheng, Y. C.; Huang, Y. J.; Tsai, C. H. *Catalysis Letters* **2002**, *80*, 153.

(29) Liu, A. H.; Wei, M. D.; Honma, I.; Zhou, H. S. *Analytical Chemistry* **2005**, *77*, 8068.

(30) Gao, T.; Wu, Q. L.; Fjellvag, H.; Norby, P. *Journal of Physical Chemistry C* **2008**, *112*, 8548.

(31) Chen, W. P.; Guo, X. Y.; Zhang, S. L.; Jin, Z. S. *Journal of Nanoparticle Research* **2007**, *9*, 1173.

(32) Chen, Q.; Du, G. H.; Zhang, S.; Peng, L. M. *Acta Crystallographica Section B-Structural Science* **2002**, *58*, 587.

(33) Yang, J. J.; Jin, Z. S.; Wang, X. D.; Li, W.; Zhang, J. W.; Zhang, S. L.; Guo, X. Y.; Zhang, Z. J. *Dalton Transactions* **2003**, 3898.
(34) Hulteen, J. C.; Martin, C. R. *Journal of Materials Chemistry* **1997**, *7*, 1075.
(35) Aprile, C.; Corma, A.; Garcia, H. *Physical Chemistry Chemical Physics* **2008**, *10*, 769.
(36) Ma, R. Z.; Sasaki, T.; Bando, Y. *Journal of the American Chemical Society* **2004**, *126*, 10382.
(37) Zhang, M.; Jin, Z. S.; Zhang, J. W.; Guo, X. Y.; Yang, H. J.; Li, W.; Wang, X. D.; Zhang, Z. J. *Journal of Molecular Catalysis a-Chemical* **2004**, *217*, 203.
(38) Grzmil, B.; Rabe, M.; Kic, B.; Lubkowski, K. *Industrial & Engineering Chemistry Research* **2007**, *46*, 1018.
(39) Picquart, M.; Escobar-Alarcon, L.; Torres, E.; Lopez, T.; Haro-Poniatowski, E. *Journal of Materials Science* **2002**, *37*, 3241.
(40) Toyoda, M.; Nanbu, Y.; Nakazawa, Y.; Hirano, M.; Inagaki, M. *Applied Catalysis B-Environmental* **2004**, *49*, 227.
(41) Wu, J. J.; Yu, C. C. *Journal of Physical Chemistry B* **2004**, *108*, 3377.
(42) Sakthivel, S.; Shankar, M. V.; Palanichamy, M.; Arabindoo, B.; Bahnemann, D. W.; Murugesan, V. *Water Research* **2004**, *38*, 3001.
(43) Hidalgo, M. C.; Maicu, M.; Navio, J. A.; Colon, G. *Catalysis Today* **2007**, *129*, 43.
(44) Miao, L.; Ina, Y.; Tanemura, S.; Jiang, T.; Tanemura, M.; Kaneko, K.; Toh, S.; Mori, Y. *Surface Science* **2007**, *601*, 2792.
(45) Bavykin, D. V.; Walsh, F. C. *European Journal of Inorganic Chemistry* **2009**, 977.
(46) Ma, R. Z.; Bando, Y.; Sasaki, T. *Chemical Physics Letters* **2003**, *380*, 577.
(47) Ma, R. Z.; Fukuda, K.; Sasaki, T.; Osada, M.; Bando, Y. *Journal of Physical Chemistry B* **2005**, *109*, 6210.
(48) Toledo-Antonio, J. A.; Capula, S.; Cortes-Jacome, M. A.; Angeles-Chavez, C.; Lopez-Salinas, E.; Ferrat, G.; Navarrete, J.; Escobar, J. *Journal of Physical Chemistry C* **2007**, *111*, 10799.
(49) Cavalheiro, A. A.; Bruno, J. C.; Saeki, M. J.; Valente, J. P. S.; Florentino, A. O. *Thin Solid Films* **2008**, *516*, 6240.
(50) Riss, A.; Berger, T.; Stankic, S.; Bernardi, J.; Knozinger, E.; Diwald, O. *Angewandte Chemie-International Edition* **2008**, *47*, 1496.
(51) Sun, X. M.; Li, Y. D. *Chemistry-a European Journal* **2003**, *9*, 2229.
(52) Diebold, U. *Surface Science Reports* **2003**, *48*, 53.
(53) Bellardita, M.; Addamo, M.; Di Paola, A.; Palmisano, L. *Chemical Physics* **2007**, *339*, 94.
(54) Pastoriza-Santos, I.; Liz-Marzan, L. M. *Journal of Materials Chemistry* **2008**, *18*, 1724.
(55) Schwartzberg, A. M.; Zhang, J. Z. *Journal of Physical Chemistry C* **2008**, *112*, 10323.
(56) Kumbhar, A. S.; Kinnan, M. K.; Chumanov, G. *Journal of the American Chemical Society* **2005**, *127*, 12444.
(57) Driskell, J. D.; Lipert, R. J.; Porter, M. D. *Journal of Physical Chemistry B* **2006**, *110*, 17444.
(58) Seney, C. S.; Gutzman, B. M.; Goddard, R. H. *Journal of Physical Chemistry C* **2009**, *113*, 74.
(59) Gribov, E. N.; Cocina, D.; Spoto, G.; Bordiga, S.; Ricchiardi, G.; Zecchina, A. *Physical Chemistry Chemical Physics* **2006**, *8*, 1186.
(60) Zecchina, A.; Arean, C. O.; Palomino, G. T.; Geobaldo, F.; Lamberti, C.; Spoto, G.; Bordiga, S. *Physical Chemistry Chemical Physics* **1999**, *1*, 1649.
(61) Hadjiivanov, K.; Lamotte, J.; Lavalley, J. C. *Langmuir* **1997**, *13*, 3374.
(62) Hadjiivanov, K. I.; Klissurski, D. G. *Chemical Society Reviews* **1996**, *25*, 61.
(63) Scaranto, J.; Giorgianni, S. *Journal of Molecular Structure-Theochem* **2008**, *858*, 72.
(64) Bordiga, S.; Palomino, G. T.; Arduino, D.; Lamberti, C.; Zecchina, A.; Arean, C. O. *Journal of Molecular Catalysis a-Chemical* **1999**, *146*, 97.